A Single-Stage IPT Converter with Optimal Efficiency Tracking and Constant Voltage Output Against Dynamic Variations of Coupling and Load

Zhicong Huang, *Senior Member, IEEE,* Bowei Zou, *Graduate Student Member, IEEE,* Zhenwei Huang,
Herbert Ho-Ching Iu, *Senior Member, IEEE,* and Chi K. Tse, *Fellow, IEEE*

***Abstract*—Multistage design based inductive-power-transfer (IPT) systems have been carried out to cope with power regulation and optimal efficiency tracking against variations of load conditions and coupling coefficients in dynamic scenarios like roadway-powered electric vehicles. However, it is still challenging for a single-stage IPT converter to do so, due to the fixed transfer ratio and narrow optimal load range of the resonant tank. This paper aims to fill the gap by integrating active switches within the IPT converter to extend the modulation range. A new series-series compensated IPT converter is proposed, which, unlike the conventional ones, employs two switched-controlled capacitors (SCCs) and a semi-active rectifier (SAR). The secondary SCC and the SAR cooperate via an inner control loop to emulate a null secondary impedance and an optimal load resistance, while the primary SCC is responsible for the output power regulation via an outer control loop. The operating principle enables a constant voltage output and optimal efficiency tracking against dynamic variations of coupling coefficient and load condition, while fixed operating frequency and soft switching are also permitted. Experimental results validate the performance.**

***Index Terms*—Constant Voltage, Dynamic, Inductive Power Transfer, Optimal Efficiency, Single-Stage.**

I. INTRODUCTION

The development of inductive power transfer (IPT) technology has enabled contactless power transfer over an air gap distance via magnetic coupling [1], [2]. IPT is suitable for power supply applications where physical contact is inconvenient or hazardous. In stationary scenarios, like wireless chargers for consumer electronics, mine appliances, and electric vehicles (EVs) in garages, IPT has shown significant benefits in providing safe, user-friendly, and maintenance-free operations and has become standardized in recent years [3]–[6]. In contrast to applications in stationary scenarios, IPT performs favorably in dynamic scenarios, being able to truly free the power supply, for instance, in roadway-powered EVs [7], wireless excited synchronous machines [8], biomedical implants [9] and so on. However, using IPT systems in dynamic scenarios inevitably incurs more severe parameter fluctuation, which is challenging for efficient and stable power transfer.

The loosely-coupled transformer (LCT), which is formed by the coupled transmitter and receiver coils, is essential for power transfer in IPT systems. A variety of studies have been carried out to design and optimize the LCT, aiming at improving the efficiency of wireless power transfer. The transmitter and receiver coils should first have interoperable structures in order to couple well with each other [10]. Optimization of the LCT towards a high coupling coefficient (k) and coil quality factors ensure efficient wireless power transfer [11], [12]. Design for misalignment tolerance has also been considered by using more coils to shape desired magnetic flux, such as double-D quadrature pad [13] and tripolar pad [14]. They incure additional material cost or higher manufacturing complexity.

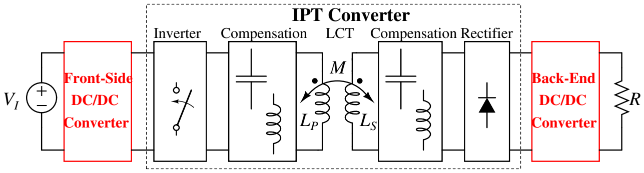

(a) Multistage designs [18]–[24]

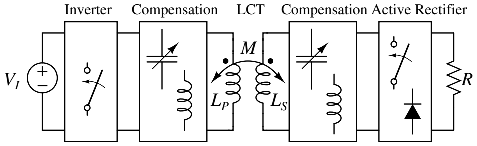

(b) Single-stage designs

Fig. 1. Diagrams of IPT systems that can achieve optimal efficiency and constant output against variations of k and load condition.

For the misalignment issues in stationary applications, k usually varies in a small range and becomes fixed during the power transfer. In contrary, continuous and severe longitudinal, lateral, angular and rotational motions occur between the transmitter and receiver coils in dynamic applications, which leads to wide-range variation of k that be fully addressed via the design of LCT. Moreover, to achieve optimal efficiency, a well-compensated LCT should be loaded at a very narrow vicinity of load condition, which has been studied and known to be k-dependent [15]–[18]. Once the well compensated LCT is not optimally loaded, which may be caused by k variation or load change, it will suffer from the dramatic efficiency degradation. Therefore, an appropriate IPT converter topology and an effective control method are needed to achieve optimal efficiency and constant output against the variations of k and load condition.

Multistage designs have been first carried out to address the above issues [18]–[24]. The diagram shown in Fig. 1(a) illustrates the operating principle of these multistage designs. In these designs, an IPT converter is cascaded with a front-end DC-DC converter and a load-side DC-DC converter. Depend-

TABLE I
Comparison of State-of-the-art Works

Desirable merits	Multistage [18]–[26]	Hopping methods [27]–[31]	Hybrid topologies [32], [33]	Dual H-bridges [34], [35]	FM+SAR [37], [38]	SCC+SAR [39]	Proposed
Constant output against load change	√	√	√	√	√	√	√
Constant output against k variation	√	×	√ (Nearly)	√	×	×	√
Load matching for optimal efficiency	√	×	×	√	√	√	√
Single-stage	×	√	√	√	√	√	√
Soft switching	×	√	√	×	√	√	√
Fixed operating frequency	√	depends	√	√	×	√	√

ing on the choice of compensation circuitry, the IPT converter can act as a voltage gain, transadmittance, current gain, or transresistance converter. For example, the four basic IPT converters with series-series, series-parallel, parallel-series and parallel-parallel compensation circuits have constant $I_{\text{Out}}/V_{\text{In}}$, $V_{\text{Out}}/V_{\text{In}}$, $I_{\text{Out}}/I_{\text{In}}$ and $V_{\text{Out}}/I_{\text{In}}$ ratios respectively [18]. Without any modulation, the efficiency and output of the IPT converter suffer from the variations of k and load condition. Thus, the load-side DC-DC converter adaptively controls the equivalent load observed by the IPT converter to track the optimal efficiency, while the input-side modulation is responsible for the front-end DC-DC converter to achieve output regulation. Different control schemes have been studied, such as the minimum input current tracking [19], the maximum efficiency tracking [20]–[23], and the voltage/current ratio control [18], [24]. Based on the above operating principle, the IPT converter is readily to track the optimal efficiency and maintain constant output under variations of k and load condition. However, additional losses and costs of the DC-DC converters are inevitable, and moreover, complex control is needed to ensure stability and fast response of the cascading DC-DC converters [25], [26].

To avoid the penalties brought by multistage designs, significant research efforts have been directed toward single-stage designs. Under a fixed k, hopping the operating frequencies [27], [28] or the compensation topologies [29]–[31] are two common ways to realize constant current (CC) or constant voltage (CV) outputs against a wide range of loads. Taking it one step further, hybrid IPT topologies, including input-parallel-output-parallel, input-parallel-output-series, input-series-output-parallel, and input-series-output-series, are constructed for a CC or CV output with misalignment tolerance [32], [33]. Nevertheless, without deep modulation in the rectifier, the above methods cannot realize load matching and optimize efficiency performance against variations of k and load condition.

With additional active switches integrated within the IPT converter, as shown in Fig. 1(b), the modulation given by the additional DC-DC converter can be alternatively implemented by the inverter and the rectifier, such that the DC-DC converters can be eliminated. However, it is still challenging to achieve wide range modulation in the input and output terminals, while implementing soft switching in the inverter and the rectifier. In [34], [35], dual H-bridges are used, and hard switching loss is allowed to extend the modulation range of the inverter and rectifier, without changing the resonance condition of the resonant tank circuit, so as to achieve output regulation and load matching against variations of k and load condition. It is noteworthy that the efficiency degrades significantly with the increase of modulation depth. Soft-switching modulation of voltage-controlled and current-controlled semi-active rectifiers (SARs) has been investigated [36], [37]. These SARs transform the load into an equivalent impedance that includes not only a resistive component but also a reactive component. They provide control freedom for load matching but may also worsen the resonance condition in the secondary. To address this issue, frequency modulation (FM) in the primary cooperates with the load transformation to simultaneously realize load matching and a CC or CV output [37], [38]. Nevertheless, it cannot cope with the dynamic k variation or misalignment issues, and thus more control freedom is desired for the IPT systems. The switch-controlled capacitor (SCC) technique is found to be another way to cancel the undesired reactance generated by the SARs, so as to maintain the resonance condition in the secondary [39]. Without any modulation in the primary, the proposed wireless power supply in [39] can maintain maximum efficiency against load change but still fails to cope with the dynamic k variation or misalignment issues.

To the best of our knowledge, an IPT converter that features the following merits has not yet been developed, as summarized in Table I.

1) Single-stage design
2) CV output and optimal efficiency tracking against dynamic variations of k and load condition
3) Soft switching and fixed operating frequency

To fill the gap, this paper proposes a series-series compensated IPT converter, which, unlike the conventional ones, employs two SCCs and a semi-active rectifier. The operating principles, including k-indepdent criteria for optimal efficiency and regulation of output power, are first introduced in Section II, based on which, the schematic, modulation, and control of the proposed IPT converter are detailed in Section III. The performances of the proposed IPT converter are experimentally verified in Section IV. Finally, Section V concludes this paper.

II. Operating Principle

An equivalent circuit model of the widely-used series-series compensated IPT converter is shown in Fig. 2. As usual, the loosely-coupled transformer has primary self-inductance L_P, secondary self-inductance L_S and mutual inductance M. The coupling coefficient is given by $k = M/\sqrt{L_P L_S}$. R_P and R_S are equivalent series resistors that represent losses in the

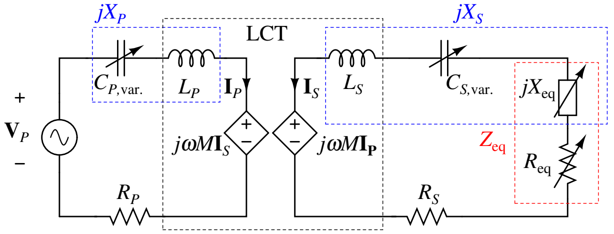

Fig. 2. General equivalent circuit model of the widely-used series-series compensated IPT converter.

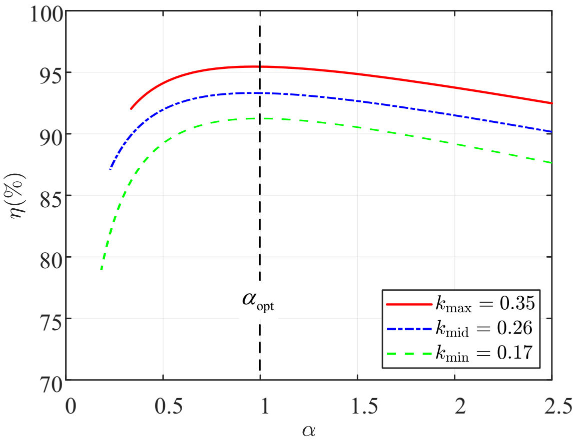

Fig. 3. Efficiency η versus current ratio α under different values of k. (Parameters used for simulation are: $L_P = 147.23$ μH, $L_S = 148.5$ μH, $R_P = 0.4$ Ω, and $R_S = 0.4$ Ω. Unless specified, they will be used for the rest simulation.)

primary and secondary respectively. For a more general discussion, the primary and secondary compensation capacitors are both variables, denoted as $C_{P,\text{var.}}$ and $C_{S,\text{var.}}$ respectively, while the load is an impedance that includes resistive and reactive components, given by $Z_{\text{eq}} = R_{\text{eq}} + jX_{\text{eq}}$. Implementation of variable $C_{P,\text{var.}}$, $C_{S,\text{var.}}$ and Z_{eq} will be detailed in subsequent sections. v_p, i_p, v_s and i_s are fundamental components, and $\mathbf{V}_P$, $\mathbf{I}_P$, $\mathbf{V}_S$ and $\mathbf{I}_S$ are vector representation of fundamental components respectively. Circuit equations are

$$\mathbf{V}_P = \mathbf{I}_P(jX_P + R_P) + jX_M\mathbf{I}_S, \text{ and} \tag{1}$$

$$-\mathbf{I}_S R_{\text{eq}} = \mathbf{I}_S(jX_S + R_S) + jX_M\mathbf{I}_P, \tag{2}$$

where

$$X_P = \omega L_P - \frac{1}{\omega C_{P,\text{var.}}}, \tag{3}$$

$$X_S = \omega L_S - \frac{1}{\omega C_{S,\text{var.}}} + X_{\text{eq}}, \text{ and} \tag{4}$$

$$X_M = \omega M. \tag{5}$$

A. k-Independent Criteria for Optimal Efficiency

The efficiency η can be calculated by (6). By substituting (1) to (5) into (6), η can be expressed by (7). As a high-quality IPT converter usually satisfies $X_M^2/(R_P R_S) \gg 1$ and $R_{\text{eq}}/R_S \gg 1$ [38], (7) can be further simplified as (8).

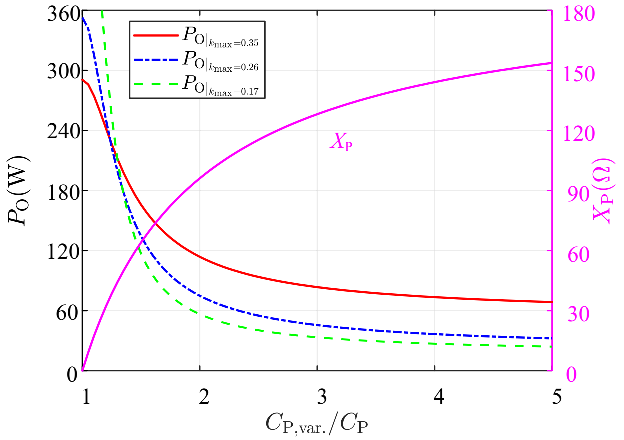

Fig. 4. Output power P_O and primary reactance X_P versus primary compensation capacitor $C_{P,\text{var.}}$.

$$\eta = \frac{|\mathbf{I}_S|^2 R_{\text{eq}}}{|\mathbf{I}_S|^2 (R_{\text{eq}} + R_S) + |\mathbf{I}_P|^2 R_P} \tag{6}$$

$$= \frac{X_M^2 R_{\text{eq}}}{\left[(R_{\text{eq}} + R_S)^2 + X_S^2\right] R_P + X_M^2 (R_{\text{eq}} + R_S)} \tag{7}$$

$$\approx \frac{1}{\frac{R_{\text{eq}} + \frac{X_S^2}{R_{\text{eq}}}}{X_M^2} R_P + \frac{R_S}{R_{\text{eq}}} + 1} \tag{8}$$

Optimum values of R_{eq} and X_{S} that achieve maximum efficiency can be found from (8). If the operating frequency ω is fixed, by solving the partial differentials $\frac{\partial \eta}{\partial X_S} = 0$ and $\frac{\partial \eta}{\partial R_{\text{eq}}} = 0$, optimal efficiency $\eta_{\max}$ can be achieved as

$$\eta_{\text{opt}} = \frac{1}{\frac{2}{Q_P Q_S} + 1}, \text{ if} \tag{9}$$

$$X_{S,\text{opt}} = \omega L_S - \frac{1}{\omega C_{S,\text{var.}}} + X_{\text{eq}} = 0, \text{ and} \tag{10}$$

$$R_{\text{eq,opt}} = X_M \sqrt{\frac{R_S}{R_P}}. \tag{11}$$

where $Q_P = (\omega L_P)/R_P$ and $Q_S = (\omega L_S)/R_S$ are quality factor representation. Criteria for maximum efficiency given in (10) and (11) indicate that the secondary resonant tank should have null equivalent reactance and the equivalent load resistance should be matching.

From (10), null secondary reactance can be maintained by varying $C_{S,\text{var.}}$ to offset X_{eq}. From (11), it can be observed that $R_{\text{eq,opt}}$ is k-dependent and thus should be correspondingly varied with the change of k for optimal efficiency in dynamic scenarios. However, since it is difficult to directly detect k in practice, a viable condition for optimal efficiency should be derived. Given null secondary reactance can be satisfied, i.e., (10) is satisfied, the amplitude ratio of secondary-side current to primary-side current can be defined as

$$\alpha = \left|\frac{\mathbf{I}_S}{\mathbf{I}_P}\right| = \frac{X_M}{(R_{\text{eq}} + R_S)}. \tag{12}$$

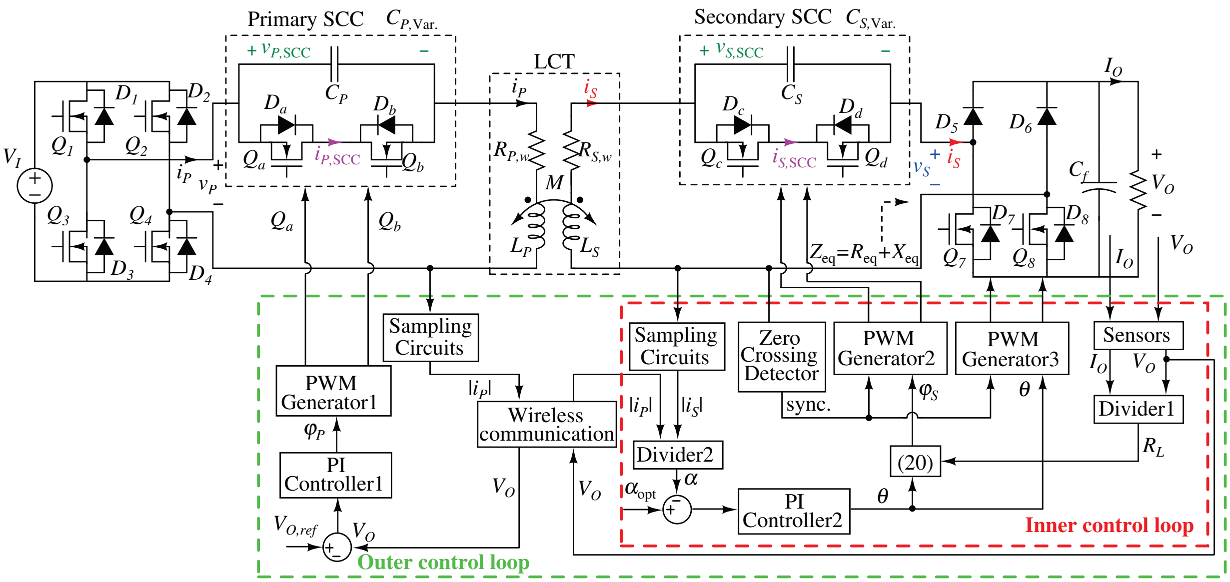

Fig. 5. Schematics and control diagram of the proposed IPT converter.

With (6) and (12), typical curves of efficiency η versus current ratio α are plotted in Fig. 3. It can be observed that there are efficiency peaks under different values of k. By substituting $X_{S,\text{opt}}$ and $R_{\text{eq,opt}}$ given by (10) and (11) into (2), the optimal α can be derived as

$$\alpha_{\text{opt}} = \left|\frac{\mathbf{I}_S}{\mathbf{I}_P}\right| \approx \sqrt{\frac{R_P}{R_S}}. \tag{13}$$

Here, (13) represents the k-independent criterion that can achieve the optimal efficiency regardless of k. This means that direct detection of the coupling coefficient is not needed in the proposed scheme, which is an advantage over existing methods. As shown in Fig. 3, if α is maintained at α_{opt}, the IPT converter can always operate at its optimal efficiency under different k. Since the current amplitudes can be readily detected, (13) is a viable condition for tracking the optimal efficiency. It is worth noting that the proposed control scheme relies on the amplitude information, while the phase information of these currents is not necessary. Thus, it offers practical advantages and simplifies the implementation of current sampling.

B. Regulation of Output Power

In addition to maintaining optimal efficiency, wide-range output power is desired in dynamic IPT. Since the modulation in the secondary has been responsible for the optimal efficiency, primary-side tuning will be investigated for the regulation of output power. Assuming $R_P = R_S = 0$, i.e., lossless power transfer, the output power can be derived with (1), (2), (10) and (11), and it is given by

$$P_O = \left|\frac{\mathbf{I}_S}{\sqrt{2}}\right|^2 R_{\text{eq,opt}} = \frac{|\mathbf{V}_P|^2 X_M}{2(X_P^2 + X_M^2)}. \tag{14}$$

If the operating frequency ω is fixed, P_O can only be regulated via the change of X_P. According to (3), variable $C_{P,\text{var.}}$ is therefore required. Fig. 4 shows the output power P_O together with the primary reactance X_P along with the variation of primary compensation capacitor $C_{P,\text{var.}}$. Wide-range output power can be readily achieved by varying $C_{P,\text{var.}}$.

III. SCHEMATIC, MODULATION AND CONTROL OF THE PROPOSED SINGLE-STAGE IPT CONVERTER

A. Schematic

Based on the fundamental circuit model shown by Fig. 2 and the operating principle illustrated in Section II, a single-stage IPT converter is proposed as depicted in Fig. 5. It includes a full-bridge inverter, two switch-controlled capacitors (SCCs), an LCT and a semi-active rectifier (SAR). The SAR is used to transform the load resistance R_L that varies in a wide range into the optimal value $R_{\text{eq,opt}}$ for the optimal efficiency η_{opt} according to (11). However, to realize soft-switching modulation in the SAR, which will be detailed in Section III-B, a variable equivalent impedance X_{eq} that violates (10) will be incurred with the variation of R_L. The secondary SCC helps to offset X_{eq}, such that (10) can be obeyed for optimal efficiency. Another control variable for output power regulation is introduced by the primary SCC.

B. Soft-Switched Modulations and Models of SAR and SCC

The SAR has two diodes (D_5, D_7) in the upper legs and two MOSFET switches (Q_6, Q_8) in the lower legs. The switching sequences and the operating waveforms of the SAR are shown in Fig. 6. Q_6 and Q_8 are used to control the conduction angle of v_S denoted by θ, and they complement each other. Q_6 is turned ON for half a cycle with a phase delay $(\pi - \theta) \in [0, \pi]$ to the zero-crossing point where i_S commutates from negative to positive. Then, Q_8 operates in a similar way. The zero-crossing detection can be implemented by using a current transformer and comparators, and the zero-crossing signal is then used to trigger the ePWM module of the TMS320F28335 DSP controller to synchronize the PWM generation. The

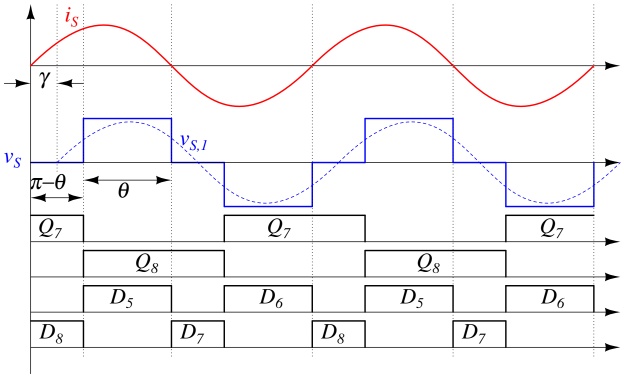

Fig. 6. Switching sequences and operating waveforms of the SAR.

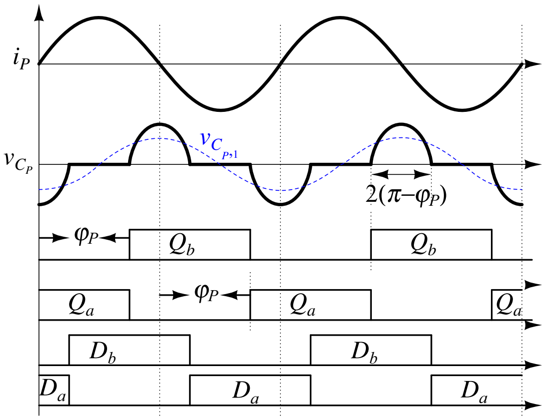

Fig. 7. Switching sequences and operating waveforms of the SCCs.

ePWM module of the TMS320F28335 DSP controller uses a 150 MHz clock and can capture the 85 kHz zero-crossing signal. The conduction angle θ of the SAR ranges from 0 to a maximum π, i.e., $\theta \in [0, \pi]$. It can be observed that Q_6 and Q_8 are turned ON during the ON-time of their antiparallel diodes to enjoy zero-voltage switching (ZVS). The change of θ will lead to a phase angle between v_S and i_S. As shown by the dashed blue curve in Fig. 6, $v_{S,1}$ is the fundamental component of v_S, and it lags i_S with a phase angle given by $\gamma = \frac{\pi-\theta}{2}$. Therefore, the equivalent load is an impedance rather than a pure resistance, as given by (15)–(17). The derivation can be found in [36], [38], [40].

$$Z_{\text{eq}} = R_{\text{eq}} + jX_{\text{eq}}, \ \text{where} \tag{15}$$

$$R_{\text{eq}} = \frac{8}{\pi^2} R_L \sin^4(\frac{\theta}{2}), \ \text{and} \tag{16}$$

$$X_{\text{eq}} = -\frac{8}{\pi^2} R_L \sin^3(\frac{\theta}{2}) \cos(\frac{\theta}{2}). \tag{17}$$

Considering the similarity in operational principles between the primary and secondary SCC modules, the primary SCC is employed as an example to illustrate the operating mechanism. The primary SCC consists of a capacitor C_P in parallel with two anti-connected MOSFET switches Q_a and Q_b. The switching sequences and the operating waveforms of the SCC are shown in Fig. 7. Q_a and Q_b are used to shape the terminal voltage of C_P, and they complement each other. Q_b has a phase shift $\varphi_P \in [\frac{\pi}{2}, \pi]$ from the zero-crossing point where i_P commutates from negative to positive. Then, Q_a operates in a similar way. Q_a and Q_b are turned ON and OFF at zero voltage for low switching loss. v_{C_P} is shaped as part of a sine wave, and the effective charging/discharging time of C_P in half a cycle is $2(\pi - \varphi_P)$. As the dashed curve labeled with $v_{C_P,1}$ shows, the increase of φ_P will decrease the peak of the fundamental component of v_{C_P}. Consequently, the equivalent capacitance $C_{P,\text{var.}}$ of the SCC can be varied by the phase shift angle φ_P. Equivalent $C_{P,\text{var.}}$ has been studied and given by (18) [41], [42], and it can be simplified as a polynomial given by (19) for easy calculation.

$$C_{P,\text{var.}} = \frac{C_P}{2 - \frac{2\varphi_P - \sin 2\varphi_P}{\pi}} \tag{18}$$

$$\approx \frac{\pi^2}{4(\varphi_P - \pi)^2} C_P. \tag{19}$$

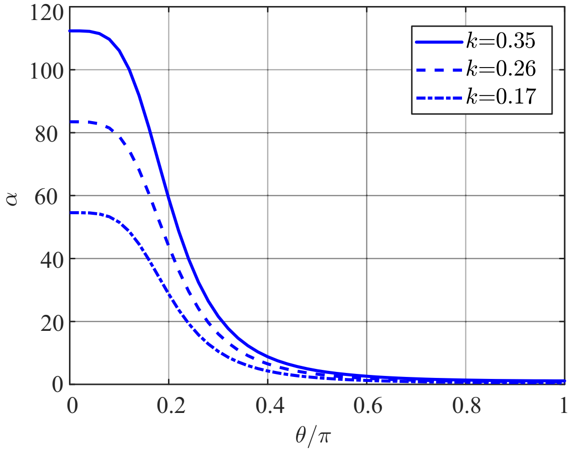

Fig. 8. α versus θ under different coupling coefficients.

C. Inner Loop Control for Optimal Efficiency

The objective of the secondary SCC is to cancel the equivalent load reactance X_{eq} generated by the SAR and maintain null reactance in the secondary. To satisfy (10), φ_S should be cooperatively varied with θ. With (10), (17) and (19), the expression of phase-shift angle φ_S can be derived as (20).

$$\varphi_S = \pi - \frac{\pi}{2}\sqrt{C_S\left(\omega_0^2 L_S - \omega_0 \frac{8}{\pi^2} \sin^3\frac{\theta}{2} \cos\frac{\theta}{2} R_L\right)} \tag{20}$$

With X_{eq} being canceled by the secondary SCC, the SAR is responsible for transforming R_L into $R_{\text{eq,opt}}$ by varying the conduction angle θ of the SAR. However, it is difficult to observe R_{eq} directly. Alternatively, as demonstrated in Section II-A, it is readily to observe the current ratio $\alpha = |\mathbf{I}_S/\mathbf{I}_P|$, and once α is tightly regulated as $\alpha_{\text{opt}} \approx \sqrt{\frac{R_P}{R_S}}$ given in (13), $R_{\text{eq,opt}}$ can be achieved regardless of k variation. Therefore, θ is controlled to achieve α_{opt}. Only the amplitude of the high-frequency current is needed for the control, and the sampling rate is the same as the control frequency of the inner loop, which is far lower than the resonant frequency. Thus, there is no difficulty in the current measurement.

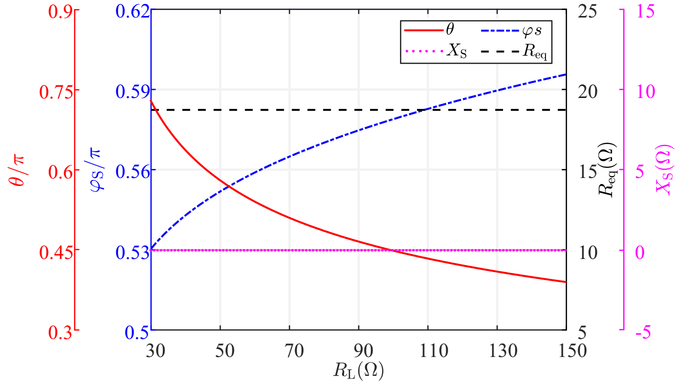

Fig. 9. φ_S, θ, R_{eq} and X_S versus R_L ($k = 0.26$).

Moreover, by solving the partial differential given in (21), it can be found that α monotonically decreases with the increase of θ as shown in Fig 8. Such that, a linear controller can be used to regulate θ.

$$\frac{\partial\alpha}{\partial\theta} = -\frac{\pi^2\omega_0 M}{16R_L\sin^5(\frac{\theta}{2})}\cos(\frac{\theta}{2}) < 0, \text{ for } \theta \in [0,\pi]. \tag{21}$$

In practice, α_{opt} should be precisely evaluated by including the losses of all switches into consideration. To make the key contents more concise, a detailed evaluation is given in the Appendix. It can be known that the practical α_{opt} for our experimental prototype is around 0.9. Therefore, $\alpha_{\text{opt}} = 0.9$ is used as the control reference.

As depicted in Fig. 9, the cooperation of the SAR and the secondary SCC meets the requirements of optimal efficiency under variations of k and load condition. The diagram of inner loop control can be designed and implemented as shown in the red box in Fig. 5. The output voltage V_O and output current I_O can be measured by sensors, and R_L can be calculated with a divider. Current transformers together with rectifiers are used to sample $\mathbf{I}_P$ and $\mathbf{I}_S$, which are DC values. Wireless communication is used to transmit the value of $\mathbf{I}_P$ from the primary to the secondary for the calculation of α. A simple PI controller is used to correct the difference between α and α_{opt}. The PI controller generates the control signal, i.e., the conduction angle θ, for the SAR. Meanwhile, the phase-shift angle φ_S of the secondary SCC is generated according to (20).

D. Outer-Loop Control for Constant Voltage Output

Modulation of the primary SCC is similar to that of the secondary SCC, and thus it will not be repeated. The equivalent capacitance of the primary SCC is given by (22), where φ_P is the phase-shift angle of the primary SCC.

$$C_{P,\text{var.}} \approx \frac{\pi^2}{4(\varphi_P - \pi)^2}C_P \tag{22}$$

The primary reactance is therefore can be calculated by (23).

$$X_P = \omega L_P - \frac{4\left(\varphi_P - \pi\right)^2}{\pi^2\omega C_P} \tag{23}$$

Under the cooperation of the SAR and the secondary SCC, the output power of the proposed system has be derived in (14). With (14) and (23), the output voltage of the proposed system can be calculated by (24).

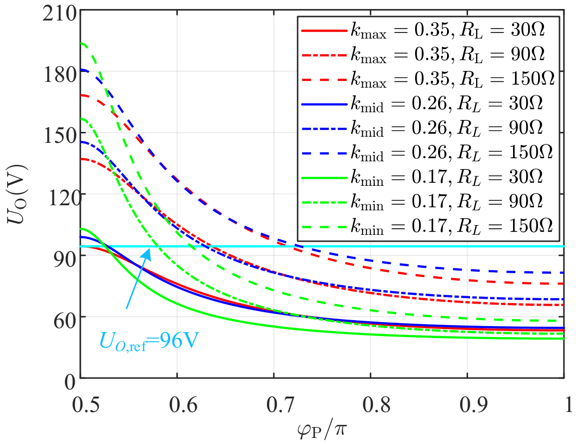

Fig. 10. V_O versus the phase-shift angle φ_P of the primary SCC.

$$V_O = \sqrt{P_O R_L} = \frac{2\sqrt{2}}{\pi}V_I\sqrt{\frac{R_{\text{eq,opt}}R_L}{X_P^2 + R_{\text{eq,opt}}^2}} \tag{24}$$

From (24), φ_P should be tightly regulated to maintain a CV output against the variations of k and load condition. By solving the partial differential (25), V_O monotonically decreases with the increase of φ_P, which is regardless of coupling coefficient k and load condition R_L.

$$\begin{aligned}\frac{\partial V_O}{\partial\varphi_P} &= \frac{16\sqrt{2}V_I X_P\sqrt{R_{\text{eq,opt}}R_L}(\varphi_P - \pi)}{\omega_0\pi^3 C_P\sqrt{X_P^2 + R_{\text{eq,opt}}^2}} \\ &< 0, \text{ for } \varphi_P \in [\pi/2, \pi].\end{aligned} \tag{25}$$

Fig 10 shows the simulated curves of V_O versus φ_P, and it also validates the monotonicity. Therefore, as shown in the green box in Fig. 5, another PI controller is readily implemented for the output voltage regulation in the outer control loop. The DC value of V_O is sampled in the secondary and wirelessly transmitted to the primary, and the PI controller corrects the difference between V_O and its reference $V_{O,\text{ref.}}$. The output of the PI controller is used to generates the phase-shift angle φ_P for the primary SCC.

IV. EXPERIMENTAL RESULTS

To verify the optimal efficiency tracking and CV output against variations of k and load condition, an experimental prototype is built as shown by Fig. 11. The system parameters are listed in Table II. The primary-side pad is fixed, while the horizontal displacement between the secondary-side pad and the primary-side pad is adjusted by rotating the rocker. The displacement ranges from 0 mm to 52 mm, and the coupling coefficient k varies from 0.35 to 0.17 correspondingly. An electronic load is used. Efficiency measurement is performed by Yokogawa WT1803E Precision Power Scope.

A. Steady-State Waveforms

Without loss of generality, the coupling coefficient is set at $k = 0.26$. Fig. 12 shows the steady-state waveforms under

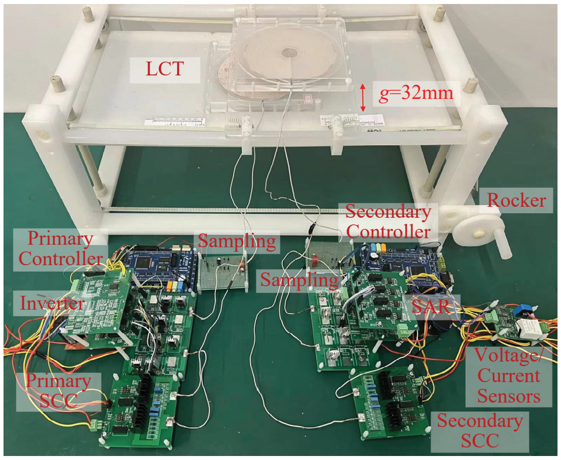

Fig. 11. Experimental prototype.

TABLE II
SYSTEM PARAMETERS

Parameters	Symbols	Measured Values
Input voltage	V_I	98 V
Swithches	Q_1-Q_4, Q_7, Q_8	IPW65R190CFD with $R_{on} \approx 0.171\Omega$ and $V_F \approx 0.7\ V$
	Q_a, Q_b, Q_c, Q_d	SCT4045DR with $R_{on} \approx 0.045\Omega$ and $V_F \approx 3.0\ V$
Diodes	D_5, D_6	MBR20200CT with $V_F \approx 0.9\ V$
Number of turns	N	34
Inner diameter	d_i	34 mm
Outer diameter	d_o	152 mm
Air gap distance	g	32 mm
Self inductance	L_P, L_S	147.23 μH, 148.5 μH
Coil resistance	$R_{P,w}$, $R_{S,w}$	0.246Ω, 0.3Ω
Coupling coefficient	k	0.17 ˜ 0.35
Primary compensation	C_P	25.68 nF
Secondary compensation	C_S	25.4 nF
Operating frequency	$\frac{\omega}{2\pi}$	85 kHz
Load	R_L	30Ω-150Ω

different load conditions. One 6-channel oscilloscope is used to capture the waveforms of the inverter, the primary SCC, the SAR, and the secondary SCC. Against the increase of load resistance, the phase difference between the primary current i_P and the secondary current i_S is fixed at 0.5π, which means the secondary side is fully compensated. The conduction angle θ of the SAR, phase-shift angle φ_S of the secondary SCC and phase-shift angle φ_P of the primary SCC can be observed. The waveforms are therefore consistent with the operating principle illustrated in Section III-B. Soft switching is permitted in the primary SCC, the secondary SCC and the SAR. Since the proposed IPT converter generates a constant voltage (96 V) and operates over a wide range of load resistance (from 30 Ω to 150 Ω), the range of output power is wide. The reactive power in the primary is utilized to facilitate the wide-range output power, but would not lead to an increase in voltage-ampere capacity of the IPT converter and hence would not harm the efficiency performance, as evidenced by (9)–(11).

B. *Measured Efficiency and Current Ratio*

The SAR and the secondary SCC are set to have close cooperation, which means the reactance generated by the SAR is canceled by the SCC via the control of φ_S. Such that, the secondary has null reactance, and there is only variation of equivalent load resistance R_{eq}. The variation of R_{eq} leads to different values of current ratio α. Efficiency curves versus α under different coupling coefficients are measured and plotted in Fig. 14. It can be observed that optimal efficiency can be achieved around $\alpha = 0.9$ under all coupling coefficients and load conditions. It is consistent with the analysis in the Appendix, and $\alpha = 0.9$ can be set as the control reference for the inner loop control. Furthermore, to clearly understand the practical distributed losses of the IPT system, the system power losses are measured and calculated for different cases. In Fig. 15, power loss breakdown of secondary-side SCC, SAR, coupling coils, primary-side SCC and inverter are represented by $P_{S,\text{SCC}}$, P_{sar}, P_{i}, $P_{P,\text{SCC}}$ and P_{inv}, respectively. The output voltage of the IPT system is maintained as 96 V, while the coupling coefficient and load resistance vary from 0.17 to 0.35 and from 30 Ω to 150 Ω respectively. It can be observed that the absolute power losses decrease with the decrease of the output power but it comprises a larger proportion, such that the maximum efficiency degrades in lighter load conditions.

C. *Transient Waveforms Under Changing Coupling and Load*

The transient waveforms under step load change for different values of k are shown in Fig. 16. Here, CH1 and CH2 are input AC voltage v_P and primary side current i_P, respectively. The DC output voltage V_O, output current I_O and secondary current i_S are measured in CH5 (brown), CH6 (orange) and CH7 (magenta), respectively. The load resistance is stepped between 30 Ω and 90 Ω. It can be observed that the current ratio is tightly regulated against step load change, and it is fixed at 0.9 via an inner loop control. The output voltage V_O is tightly regulated at 96 V via an outer loop control.

The transient waveforms under varying coupling coefficient in different load conditions are shown in Fig. 17. The coupling coefficient k is varied from 0.35 to 0.17 and back to 0.35 by slowly changing the displacement of the secondary pad to the primary pad. Similarly, CH1 (red) and CH2 (green) measure the input AC voltage v_P and primary side current i_P, respectively. The DC output voltage V_O, output current I_O and secondary current i_S are measured and shown in CH5 (brown), CH6 (orange) and CH7 (magenta), respectively. The current ratio α and the output voltage V_O are still tightly regulated as 0.9 and 96 V against the variation of the coupling coefficient via an inner loop and an outer loop control, respectively.

Therefore, these three sets of experiments validate the optimal efficiency tracking and CV output against variations of k and load conditions.

V. CONCLUDSION

A single-stage series-series compensated inductive-power-transfer converter with two switch-controlled capacitors and a semi-active rectifier is proposed to cope with power regulation and optimal efficiency tracking against variations of k and load

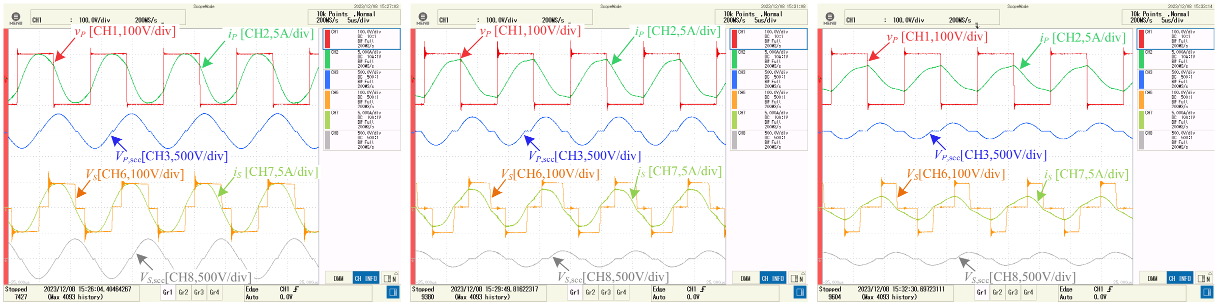

(a) $R_L = 30\ \Omega$ (b) $R_L = 90\ \Omega$ (c) $R_L = 150\ \Omega$

Fig. 12. Measured steady-state waveforms under different load conditions with coupling coefficient $k = 0.26$.

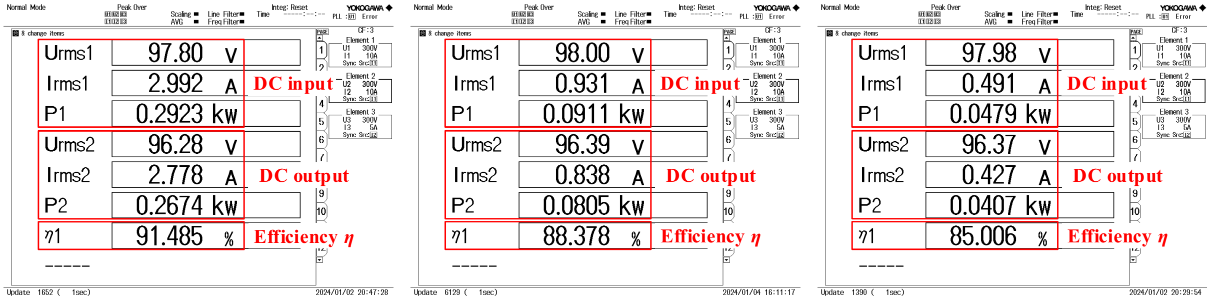

Urms1 97.80 V
Irms1 2.992 A
P1 0.2923 kW
DC input
Urms2 96.28 V
Irms2 2.778 A
P2 0.2674 kW
DC output
η1 91.485 %
Efficiency η
Update 1652 (1sec) 2024/01/02 20:47:28

Urms1 98.00 V
Irms1 0.931 A
P1 0.0911 kW
DC input
Urms2 96.39 V
Irms2 0.838 A
P2 0.0805 kW
DC output
η1 88.378 %
Efficiency η
Update 6129 (1sec) 2024/01/04 16:11:17

Urms1 97.98 V
Irms1 0.491 A
P1 0.0479 kW
DC input
Urms2 96.37 V
Irms2 0.427 A
P2 0.0407 kW
DC output
η1 85.006 %
Efficiency η
Update 1390 (1sec) 2024/01/02 20:29:54

(a) $R_L = 30\ \Omega$ (b) $R_L = 90\ \Omega$ (c) $R_L = 150\ \Omega$

Fig. 13. Measured steady-state experimental input power, output power and efficiency under different load conditions with coupling coefficient $k = 0.26$.

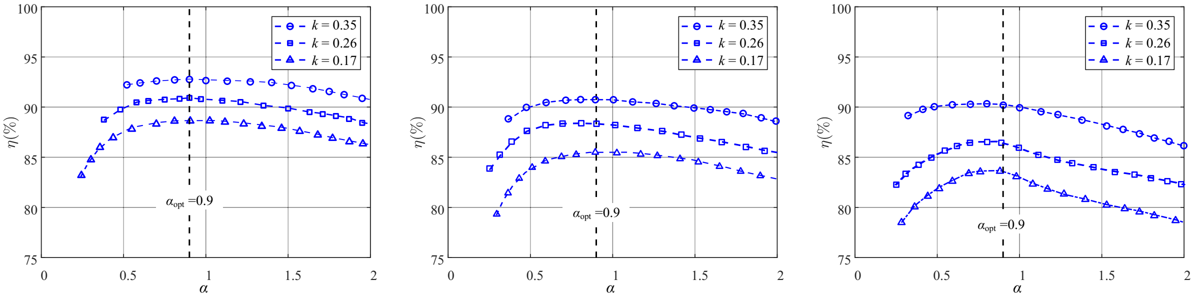

(a) $R_L = 60\ \Omega$ (b) $R_L = 90\ \Omega$ (c) $R_L = 120\ \Omega$

Fig. 14. Measured efficiency versus α under different coupling coefficients and load conditions.

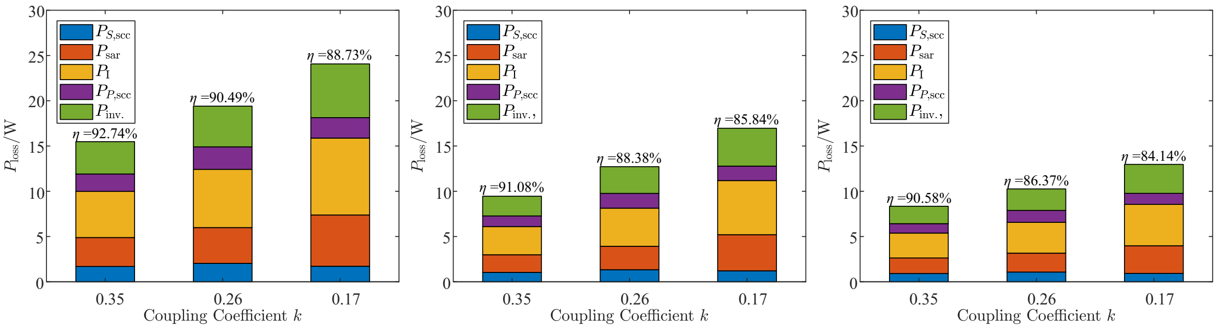

(a) Power loss breakdown for R_{L}=60 Ω for different coupling coefficients. (b) Power loss breakdown for R_{L}=90 Ω for different coupling coefficients. (c) Power loss breakdown for R_{L}=120 Ω for different coupling coefficients.

Fig. 15. Power loss breakdown of the proposed single-stage IPT.

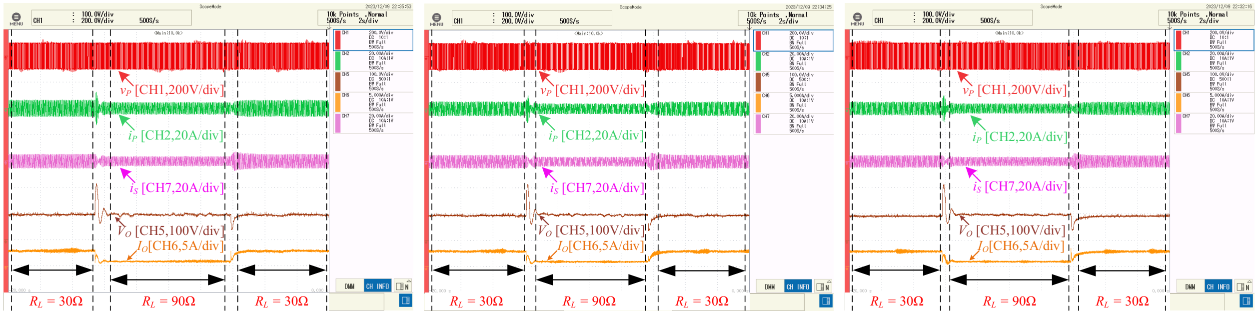

(a) $k = 0.17$ (b) $k = 0.26$ (c) $k = 0.35$

Fig. 16. Transient waveforms against step load change under different coupling coefficients.

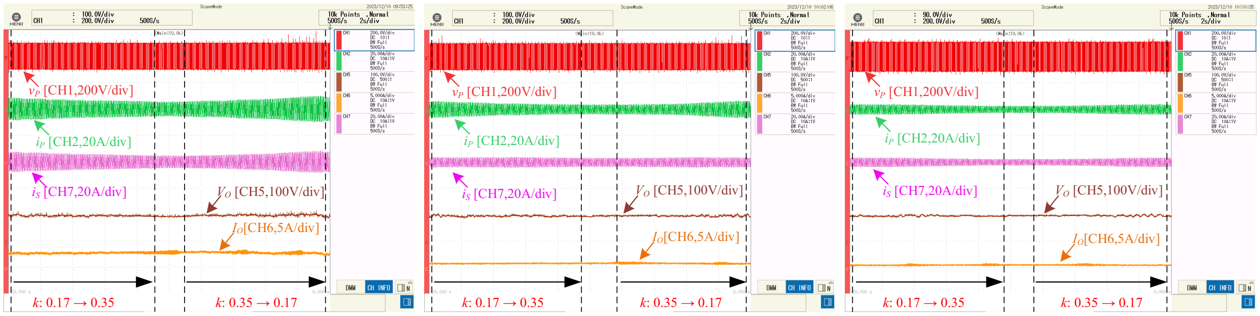

(a) $R_L = 30\ \Omega$ (b) $R_L = 90\ \Omega$ (c) $R_L = 150\ \Omega$

Fig. 17. Transient waveforms against variation of coupling coefficient under different load conditions.

conditions. The operating principle is detailed and a two-loop control scheme is used to achieve a constant voltage output and track the optimal efficiency. Steady-state waveforms and transient responses are experimentally measured to validate the performance.

APPENDIX

The power losses in the full-bridge inverter, the primary SCC and the primary coil should be considered to estimate R_P. Likewise, R_S epresents losses in the secondary coil, the secondary SCC and the SAR. To estimate R_P and R_S, the power losses in the primary SCC, secondary SCC and the SAR should be calculated.

A. Calculation of R_P

According to the operating waveforms and switching sequence shown in Fig. 7, since the primary SCC realize soft switching, only conduction loss will be considered and it can be calculated by

$$P_{P,\mathrm{SCC}} = I^2_{P,\mathrm{SCC,RMS}} R_{\mathrm{on},2} + I_{P,\mathrm{SCC,Avg}} V_{f,2}, \tag{26}$$

where $R_{\mathrm{on},2}$ and $V_{f,2}$ are on-resistance and body-diode forward voltage of the MOSFET switches Q_a and Q_b. Besides, $I_{P,\mathrm{SCC,rms}}$ and $I_{P,\mathrm{SCC,avg}}$ are the root mean square (RMS) and average value of the current flowing through primary SCC and they can be derived by

$$I_{P,\mathrm{SCC,RMS}} = \sqrt{\frac{1}{\pi}\int_{\pi-\varphi_P}^{\varphi_P} (|\mathbf{I}_P|\sin x)^2 \mathrm{d}x}, \text{ and} \tag{27}$$

$$I_{P,\mathrm{SCC,Avg}} = \frac{1}{\pi}\int_{\pi-\varphi_P}^{\varphi_P} |\mathbf{I}_P|\sin x \mathrm{d}x, \tag{28}$$

respectively.

Therefore, the R_P can be estimated by

$$R_P = 2R_{\mathrm{on},1} + \frac{P_{P,\mathrm{SCC}}}{i^2_{P,\mathrm{RMS}}} + R_{P,w}, \tag{29}$$

where $R_{on,1}$ represents ON-resistance of the MOSFET switches (Q_1-Q_4) in the full-bridge inverter, $i_{P,\mathrm{RMS}} = |\mathbf{I}_P|/\sqrt{2}$ and $R_{P,w}$ represents the resistance of primary coil.

B. Calculation of R_S

Similar to primary-side SCC, the conduction loss of secondary-side SCC can be given by (30) to (32). $R_{\mathrm{on},3}$ and $V_{f,3}$ are ON-resistance and body-diode forward voltage of the MOSFET switches Q_c and Q_d. $I_{S,\mathrm{SCC,rms}}$ and $I_{S,\mathrm{SCC,avg}}$ are the root mean square (RMS) and average value of the current flowing through secondary SCC.

$$P_{S,\mathrm{SCC}} = I^2_{S,\mathrm{SCC,RMS}} R_{\mathrm{on},3} + I_{S,\mathrm{SCC,Avg}} V_{\mathrm{f},3} \tag{30}$$

$$I_{\mathrm{S,SCC,RMS}} = \sqrt{\frac{1}{\pi}\int_{\pi-\varphi_S}^{\varphi_S} (|\mathbf{I}_S|\sin x)^2 dx} \tag{31}$$

$$I_{\mathrm{S,SCC,Avg}} = \frac{1}{\pi}\int_{\pi-\varphi_S}^{\varphi_S} |\mathbf{I}_S|\sin x dx \tag{32}$$

Moreover, the SAR realizes soft switching as shown in Fig. 6, only the conduction loss of SAR is considered and calculated by

$$P_{\mathrm{SAR}} = i^2_{\mathrm{S,RMS}} R_{\mathrm{on},4} + i_{\mathrm{S,Avg}} V_{\mathrm{f},4} \tag{33}$$

where $R_{\mathrm{on},4}$ is the ON-resistance of the MOSFET Q_5 and Q_6 in the SAR, and $V_{f,4}$ is diode forward voltage of D_7 and D_8. $i_{s,\mathrm{RMS}} = \mathbf{I}_S/\sqrt{2}$ and $i_{s,\mathrm{Avg}} = \frac{2|\mathbf{I}_S|}{\pi}$ are the RMS value and average value of i_S flowing into the SAR respectively.

Therefore, R_S can estimated by

$$R_S = \frac{P_{\mathrm{S,SCC}} + P_{\mathrm{SAR}}}{i^2_{\mathrm{S,RMS}}} + R_{S,w}. \tag{34}$$

$R_{S,w}$ is the secondary coil resistance.

C. Calculation of Practical α_{opt}

With the parameters listed in Table II, $\alpha_{\mathrm{opt}} = \sqrt{R_P/R_S}$ versus R_L under different coupling coefficients can be calculated. However, since a slight deviation from the optimal α_{opt} will not affect the efficiency too much, as shown by Fig. 3, α_{opt} can be set as 0.9 for simplicity.

REFERENCES

[1] G. A. Covic and J. T. Boys, "Inductive power transfer," *Proc. IEEE,* vol. 101, no. 6, pp. 1276–1289, Jun. 2013.

[2] S. Lukic and Z. Pantic, "Cutting the cord: Static and dynamic inductive wireless charging of electric vehicles," *IEEE Electrific. Mag.,* vol. 1, no. 1, pp. 57–64, Sep. 2013.

[3] S. Y. R. Hui and W. W. C. Ho, "A new generation of universal contactless battery charging platform for portable consumer electronic equipment," *IEEE Trans. Power Electron.,* vol. 20, no. 3, pp. 620–627, May 2005.

[4] S. Y. Hui, "Planar wireless charging technology for portable electronic products and Qi," *Proc. IEEE,* vol. 101, no. 6, pp. 1290–1301, Jun. 2013.

[5] J. T. Boys and G. A. Covic, "The inductive power transfer story at the university of Auckland," *IEEE Circuits and Syst. Mag.,* vol. 15, no. 2, pp. 6–27, Apr. 2015.

[6] R. Bosshard and J. W. Kolar, "Inductive power transfer for electric vehicle charging: Technical challenges and tradeoffs," *IEEE Power Electron. Mag.,* vol. 3, no. 3, pp. 22–30, Sep. 2016.

[7] C. C. Mi, G. Buja, S. Y. Choi, and C. T. Rim, "Modern advances in wireless power transfer systems for roadway powered electric vehicles," *IEEE Trans. Ind. Electron.,* vol. 63, no. 10, pp. 6533–6545, Oct. 2016.

[8] J. Tang, Y. Liu, and N. Sharma, "Modeling and experimental verification of high-frequency inductive brushless exciter for electrically excited synchronous machines," *IEEE Trans. Ind. Appl.,* vol. 55, no. 5, pp. 4613–4623, Sep.-Oct. 2019.

[9] Q. Chen, S. C. Wong, C. K. Tse, and X. Ruan, "Analysis, design and control of a transcutaneous power regulator for artificial hearts," *IEEE Trans. Biomed. Circuits and Syst.,* vol. 3, no. 1, pp. 23–31, Feb. 2009.

[10] M. Ibrahim et al., "Inductive charger for electric vehicle: advanced modeling and interoperability analysis," *IEEE Trans. Power Electron.,* vol. 31, no. 12, pp. 8096–8114, Dec. 2016.

[11] M. Budhia, G. A. Covic, and J. T. Boys, "Design and optimization of circular magnetic structures for lumped inductive power transfer systems," *IEEE Trans. Power Electron.,* vol. 26, no. 11, pp. 3096–3108, Sep. 2011.

[12] W. Zhang, J. C. White, A. M. Abraham, and C. C. Mi, "Loosely coupled transformer structure and interoperability study for EV wireless charging systems," *IEEE Trans. Power Electron.,* vol. 30, no. 11, pp. 6356–6367, Nov. 2015.

[13] A. Zaheer, H. Hao, G. A. Covic, and D. Kacprzak, "Investigation of multiple decoupled coil primary pad topologies in lumped IPT systems for interoperable electric vehicle charging," *IEEE Trans. Power Electron.,* vol. 30, no. 4, pp. 1937–1955, Apr. 2015.

[14] S. Kim, G. A. Covic, and J. T. Boys, "Comparison of tripolar and circular pads for IPT charging systems," *IEEE Trans. Power Electron.,* vol. 33, no. 7, pp. 6093–6103, Jul. 2018.

[15] W. Zhang, S. C. Wong, C. K. Tse, and Q. Chen, "Analysis and comparison of secondary series and parallel compensated inductive power transfer systems operating for optimal efficiency and load-independent voltage transfer ratio," *IEEE Trans. Power Electron.,* vol. 29, no. 6, pp. 2979–2990, Jun. 2014.

[16] Y. H. Sohn, B. H. Choi, E. S. Lee, G. C. Lim, G. H. Cho, and C. T. Rim, "General unified analyses of two-capacitor inductive power transfer systems: equivalence of current-source SS and SP compensations," *IEEE Trans. Power Electron.,* vol. 30, no. 11, pp. 6030–6045, Nov. 2015.

[17] W. Zhang, S. C. Wong, C. K. Tse, and Q. Chen, "Load-independent duality of current and voltage outputs of a series or parallel compensated inductive power transfer converter with optimized efficiency," *IEEE J. Emerg. Sel. Topics. Power Electron.,* vol. 3, no. 1, pp. 137–146, Mar. 2015.

[18] Z. Huang, S. C. Wong, and C. K. Tse, "Comparison of basic inductive power transfer systems with linear control achieving optimized efficiency," *IEEE Trans. Power Electron.,* vol. 35, no. 3, pp. 3276-3286, Mar. 2020.

[19] W. X. Zhong and S. Y. R. Hui, "Maximum energy efficiency tracking for wireless power transfer systems," *IEEE Trans. Power Electron.,* vol. 30, no. 7, pp. 4025–4034, Jul. 2015.

[20] M. Fu, C. Ma, and X. Zhu, "A cascaded boost-buck converter for high efficiency wireless power transfer systems," *IEEE Trans. Ind. Informat.,* vol. 10, no. 3, pp. 1972–1980, Aug. 2014.

[21] M. Fu, H. Yin, X. Zhu, and C.Ma, "Analysis and tracking of optimal load in wireless power transfer systems," *IEEE Trans. Power Electron.,* vol. 30, no. 7, pp. 3952–3963, Jul. 2015.

[22] H. Li, J. Li, K. Wang, W. Chen, and X. Yang, "A maximum efficiency point tracking control scheme for wireless power transfer systems using magnetic resonant coupling," *IEEE Trans. Power Electron.,* vol. 30, no. 7, pp. 3998–4008, Jul. 2015.

[23] T. D. Yeo, D. Kwon, S. T. Khang, and J. W. Yu, "Design of maximum efficiency tracking control scheme for closed-loop wireless power charging system employing series resonant tank," *IEEE Trans. Power Electron.,* vol. 32, no. 1, pp. 471–478, Jan. 2017.

[24] Z. Huang, S. C. Wong, and C. K. Tse, "Control design for optimizing efficiency in inductive power transfer systems," *IEEE Trans. Power Electron.,* vol. 33, no. 5, pp. 4523–4534, May 2018.

[25] Y. Yang, W. Zhong, S. Kiratipongvoot, S. C. Tan, and S. Y. R. Hui, "Dynamic improvement of series–series compensated wireless power transfer systems using discrete sliding mode control," *IEEE Trans. Power Electron.,* vol. 33, no. 7, pp. 6351–6360, Jul. 2018.

[26] K. Li, S. C. Tan and S. Y. R. Hui, "Dynamic response and stability margin improvement of wireless power receiver systems via right-half-plane zero elimination," *IEEE Trans. Power Electron.,* vol. 36, no. 10, pp. 11196–11207, Oct. 2021.

[27] Z. Huang, S. C. Wong, and C. K. Tse, "Design of a single-stage inductive-power-transfer converter for efficient EV battery charging," *IEEE Trans. Veh. Technol.,* vol. 66, no. 7, pp. 5808–5821, Jul. 2017.

[28] V. B. Vu, D. H. Tran, and W. Choi, "Implementation of the constant current and constant voltage charge of inductive power transfer systems with the double-sided LCC compensation topology for electric vehicle battery charge applications," *IEEE Trans. Power Electron.,* vol. 33, no. 9, pp. 7398-7410, Sep. 2018.

[29] C. Auvigne, P. Germano, D. Ladas, and Y. Perriard, "A dual-topology ICPT applied to an electric vehicle battery charger," in *Proc. Int. Conf. Electr. Mach.,* Mar., 2012, pp. 2287–2292.

[30] X. Qu, H. Han, S. C. Wong, C. K. Tse, and W. Chen, "Hybrid IPT topologies with constant current or constant voltage output for battery charging applications," *IEEE Trans. Power Electron.,* vol. 30, no. 11, pp. 6329–6337, Nov. 2015.

[31] R. Mai, Y. Chen, Y. Li, Y. Zhang, G. Cao, and Z. He, "Inductive power transfer for massive electric bicycles charging based on hybrid topology switching with a single inverter," *IEEE Trans. Power Electron.,* vol. 32, no. 8, pp. 5897–5906, Aug. 2017.

[32] X. Qu, Y. Yao, D. Wang, S. C. Wong, and C. K. Tse, "A family of hybrid IPT topologies with near load-independent output and high tolerance to pad misalignment," *IEEE Trans. Power Electron.,* vol. 35, no. 7, pp. 6867-6877, Jul. 2020.

[33] L. Zhao, D. J. Thrimawithana, and U. K. Madawala, "Hybrid bidirectional wireless EV charging system tolerant to pad misalignment," *IEEE Trans. Ind. Electron.,* vol. 64, no. 9, pp. 7079-7086, Sep. 2017.

[34] T. Diekhans and R. W. De Doncker, "A dual-side controlled inductive power transfer system optimized for large coupling factor variations and partial load," *IEEE Trans. Power Electron.,* vol. 30, no. 11, pp. 6320–6328, Nov. 2015.

[35] I. Karakitsios, F. Palaiogiannis, A. Markou, and N. D. Hatziargyriou, “Optimizing the energy transfer, with a high system efficiency in dynamic inductive charging of EVs,” *IEEE Trans. Veh. Tech.,* vol. 67, no. 6, pp. 4728–4742, Jun. 2018.

[36] Q. Chen, L. Jiang, J. Hou, X. Ren, and X. Ruan, “Research on bidirectional contactless resonant converter for energy charging between EVs,” *in Proc. 39th Annu. Conf. IEEE Ind. Electron. Soc.,* Vienna, Nov. 2013, pp. 1236–1241.

[37] Z. Huang, D. Wang, and X. Qu, “A novel IPT converter with current-controlled semi-active rectifier for efficiency enhancement throughout supercapacitor charging process,,” *IEEE J. Emerg. Sel. Topics. Power Electron.,* vol. 10, no. 2, pp. 2201–2209, Apr. 2022.

[38] Z. Huang, S. C. Wong, and C. K. Tse, “An inductive-power-transfer converter with high efficiency throughout battery-charging process,” *IEEE Trans. Power Electron.,* vol. 34, no. 10, pp. 10245–10255, Oct. 2019.

[39] Z. Huang, C. S. Lam, P. I. Mak, R. P. d. S. Martins, S. C. Wong, and C. K. Tse, “A Single-stage inductive-power-transfer converter for constant-power and maximum-efficiency battery charging,” *IEEE Trans. Power Electron.,* vol. 35, no. 9, pp. 8973–8984, Sep. 2020.

[40] K. Colak, E. Asa, M. Bojarski, D. Czarkowski, and O. C. Onar, “A novel phase-shift control of semibridgeless active rectifier for wireless power transfer,” *IEEE Trans. Power Electron.,* vol. 30, no. 11, pp. 6288–6297, Nov. 2015.

[41] W. Gu and K. Harada, “A new method to regulate resonant converters,” *IEEE Trans. Power Electron.,* vol. 3, no. 4, pp. 430–439, Oct. 1988.

[42] M. Yaqoob, K. Loo, and Y. M. Lai, “Fully soft-switched dual-active-bridge series-resonant converter with switched-impedance-based power control,” *IEEE Trans. Power Electron.,* vol. 33, no. 11, pp. 9267–9281, Nov. 2018.